Article:
Al-Tameemi, H.A. and Long, H. orcid.org/0000-0003-1673-1193 (2019) Finite element simulation of subsurface initiated damage from non-metallic inclusions in wind turbine gearbox bearings. International Journal of Fatigue. ISSN 0142-1123

https://doi.org/10.1016/j.ijfatigue.2019.105347

International Journal of Fatigue

Finite Element Simulation of Subsurface Initiated Damage from Non-Metallic Inclusions in Wind Turbine Gearbox Bearings

Hamza A. Al-Tameemi and Hui Long

http://doi.org/10.1016/j.ijfatigue.2019.105347

Finite Element Simulation of Subsurface Initiated Damage from Non-Metallic Inclusions in Wind Turbine Gearbox Bearings

Hamza A. Al-Tameemi[1,2]* and Hui Long[2]

[1]Department of Mechanical Engineering, University of Baghdad, Baghdad, Iraq.

[2]Department of Mechanical Engineering, The University of Sheffield, Sheffield, UK.

*Corresponding author: Dr Hamza A. Al-Tameemi (Email: hamza.al-tameemi@coeng.uobaghdad.edu.iq, hamza.tameemi@gmail.com, Tel: +964 (0) 7707277577)

Abstract

The premature failure of wind turbine gearbox bearings significantly affects the reliability of wind turbine operation and energy production. Damage initiated from non-metallic inclusions known as White Etching Cracks (WECs) has been identified as the dominant initiation mechanism that causes the premature failure under the influence of transient events. In this study, the factors affecting the initiation of subsurface damage from non-metallic inclusions were investigated by finite element modelling. It was found that the direction of surface traction and loading-unloading cycle had a detrimental effect on stress concentration at the tips of the de-bonded non-metallic inclusions in bearing steel.

Keywords: White etching cracks, Wind turbine gearbox bearing, Non-metallic inclusions, Finite element modelling, Surface traction.

1 Introduction

It has been reported that Wind Turbine Gearbox Bearings (WTGBs) are more prone to premature failure than other components in these machines [1]. However, the root-causes for this premature failure are not fully understood. The cracks associated with steel microstructure changes known as White Etching Cracks (WECs) characterize the premature failure of WTGBs and result in flaking from the surface [2][3][4][5]. In these cracks, White Etching Area (WEA) is observed along the cracks.

The hypotheses proposed for explaining the initiation of bearing premature failures have addressed both initiation on the surface of contact in the bearing raceways and initiation under the surface. Flaws on the surface are assumed to cause the surface initiation that result in deterioration of surface damage under loading conditions [4][6][7][8][9]. It has been verified by experimental examination that material defects such as non-metallic inclusions act as WECs initiators by forming butterfly wings. These are WEA observed around the inclusion to form a shape of butterfly wings, and this is described in the literature as the subsurface damage initiation hypothesis [10][11][12]. The proposed factors influencing the initiation are the penetration of hydrogen, plastic deformation due to overloading, brittle fracture due to high traction on the surface, and unconsidered loadings, such as impact load, causing lubrication failure [13][14][15][16]. However, a clear explanation for the initiation mechanism of WECs and for the effect of transient loading, such as torque reversals, has not been established so far. Accordingly, in the current study, a Finite Element modelling was developed for an inclusion in the inner raceway of the planetary bearing. The results were correlated with metallurgical examinations presented in previous studies and this correlation aimed to understand the effect of surface traction value and direction on subsurface damage initiation.

Finite Element (FE) modelling of non-metallic inclusions inside bearing steel offers a viable solution for investigating the stress state around inclusions. Earlier studies have developed models to determine the parameters affecting the stress concentration and crack initiation due to defects such as voids and inclusions. Other models have aimed to correlate the damage observed from experimental examination, considering the stress distribution due to stress risers. In general, the models simulate

parts of the contacted bodies, the roller and the raceways, representing the contact zone. The models are two dimensional (2D) in plane strain to represents a cross-section of one of the raceways normal to the axial direction of the roller bearing or three dimensional (3D) including specific thickness in the axial direction. In some of the models, the bearing steel is modelled as a one phase homogenous material with elastic-plastic properties [17]. Others studies have modelled the material as multi-phase, with different properties [18]; and in further advanced models, a phase transformation is also included [19][20][21]. The load could be represented by a roller moving on the contact surface, however, many models represent the load between the roller and the raceways by Hertzian pressure distribution and sometimes with surface traction. The inclusion is normally represented by either a void or a partition with perfect bonding to the steel matrix. In order to obtain an insight into the range of modelling methodologies used to investigate the subsurface initiated damage from inclusions and voids, three FE models from the literature are reviewed and discussed below.

Hiraoka, et al. [17] developed a 2D model and presented the inclusion at a distance of 1.2 mm from the surface as a circular void of 5 µm diameter with and without 5 µm cracks extending at 45˚ from the void. The load was applied as a roller moving on the contact surface with maximum contact pressure of 3920 MPa. The authors compared the stress distribution around the void with a butterfly wings that formed the microstructural change around a non-metallic inclusion inclined at 45˚, as found in a rolling contact fatigue test on a thrust bearing. It was shown in their study that there was better matching when the void was attached to the cracks. Accordingly, it was assumed that cracks initiated from inclusions before the formation of WEA (butterfly wings). However, in a previous study [22], it was found that for some butterfly wings there were no micro-cracks initiated by the inclusion, and thus the assumption of pre-existing cracks was not fully representative of the butterfly wings formation.

Another 2D model was developed by M. Cerullo [23] to predict crack growth from an alumina inclusion in bearing steel. In their model, a repeated Hertzian contact pressure having a maximum value of ~1 GPa was applied to represent the load of the equivalent roller passing over the inner raceway. Also, a circular alumina inclusion or a void of 5 µm in radius was embedded with a crack of 1.5 µm length that was initiated from the inclusion or the void. Their model investigated the effect of different interactions between the inclusion and the steel matrix, as well as different crack directions. The interface between the inclusion and the matrix was modelled either as a perfect bonding or by using cohesive elements that were not allowed to fail. Their study highlighted the role of the interface between an inclusion and the steel matrix. However, this study excluded the de-bonding between the inclusion and the steel matrix, which was observed in a previous study using Atomic Force Microscopy (AFM) [22]. Also, it is expected that considerations of the effect of surface traction could also provide new insights into the crack growth rate.

Another study [20] modelled the microstructure alteration that forms butterfly wings in three dimensions. The load was applied as a Hertzian pressure distribution with a maximum value of 2 GPa and contact width of b=50 µm. This pressure moved repetitively over the contact area. A spherical inclusion of 16 µm diameter was embedded at distance of 0.5b from the surface. The inclusion was considered to be perfectly bonded to the steel matrix. A damage model based on the Continuum Damage Mechanics (CDM) [19] was used to simulate the formation of the butterfly wings in the 3D simulation. This formation occurred by transforming the martensite to ferrite, according to the CDM. The main finding of this study was the lateral expansion of the butterfly wing after reaching a certain length. This finding could explain the experimental observation of some butterfly wings without inclusions due to the removal of the inclusion that is out of the examined surface during the sectioning. This will leave butterfly wings without inclusion in the examined surface. Although their model considered many variables, it did not explain the crack formation and neglected the de-bonding between the inclusion and the steel matrix, which had been widely observed.

The previous studies reviewed here show different ways of modelling damage initiation from non-metallic inclusions. However, three important issues have not been considered in these studies. Firstly, modelling the elongated inclusions, such as MnS, is less common; secondly, the de-bonding between the inclusion and the steel matrix is not considered, although it is frequently observed; and thirdly, the extreme loading, such as high surface traction, has not been investigated, although it may be a main factor in the premature failure of WTGBs. In this study, 2D FE models have been developed to address these issues to provide an understanding for the stress state that could initiate cracking due to elongated MnS inclusion.

2 FE Modelling

The FE modelling in this study aims to provide an insight into the stress state around a MnS inclusion in bearing steel under the effect of normal and tangential loads on the surface of contact between the roller and inner raceway of a bearing. This could clarify the mechanism of subsurface initiated damage, of WEA and micro-cracks, from non-metallic inclusions.

2.1 Models description:

The development of the FE models was based on the dimensions of the NREL 750 kW Wind Turbine (WT) planetary bearings that is shown in Figure 1. To investigate the premature failure occurs in the loaded zone of inner raceway in planetary bearings, only the part under the maximum load in this zone was modelled. The models were mainly the plane strain of Two Dimensional (2D) cross section in the circumferential direction of the inner raceway as shown in Figure 1. This represents a section of the inner raceway with Hertzian pressure distribution on the surface, to characterise contact with the roller under the maximum rolling element load Q_0. The inclusion was represented by an ellipse of a certain dimension, depth and inclusion-steel matrix interaction properties. In addition to the normal contact pressure, surface traction with Hertzian distribution was also applied to some of these models. The dimensions of the model, such as the thickness of the inner raceway, are identical to those in the actual bearing. The angle of the sector for the geometry in the model was chosen to be the angle that covers the effect of the roller under the maximum rolling element load Q_0 which equals to 360°/number of rollers. The mechanical properties for bearing steel according to different standards are shown in Table 1 and the chemical compositions are shown in Table 2. The properties of the bearing steel used in the models are: v=0.3, E=210 GPa, yield stress=1786 MPa, and the stress-strain curve shown in Figure 2 [24]

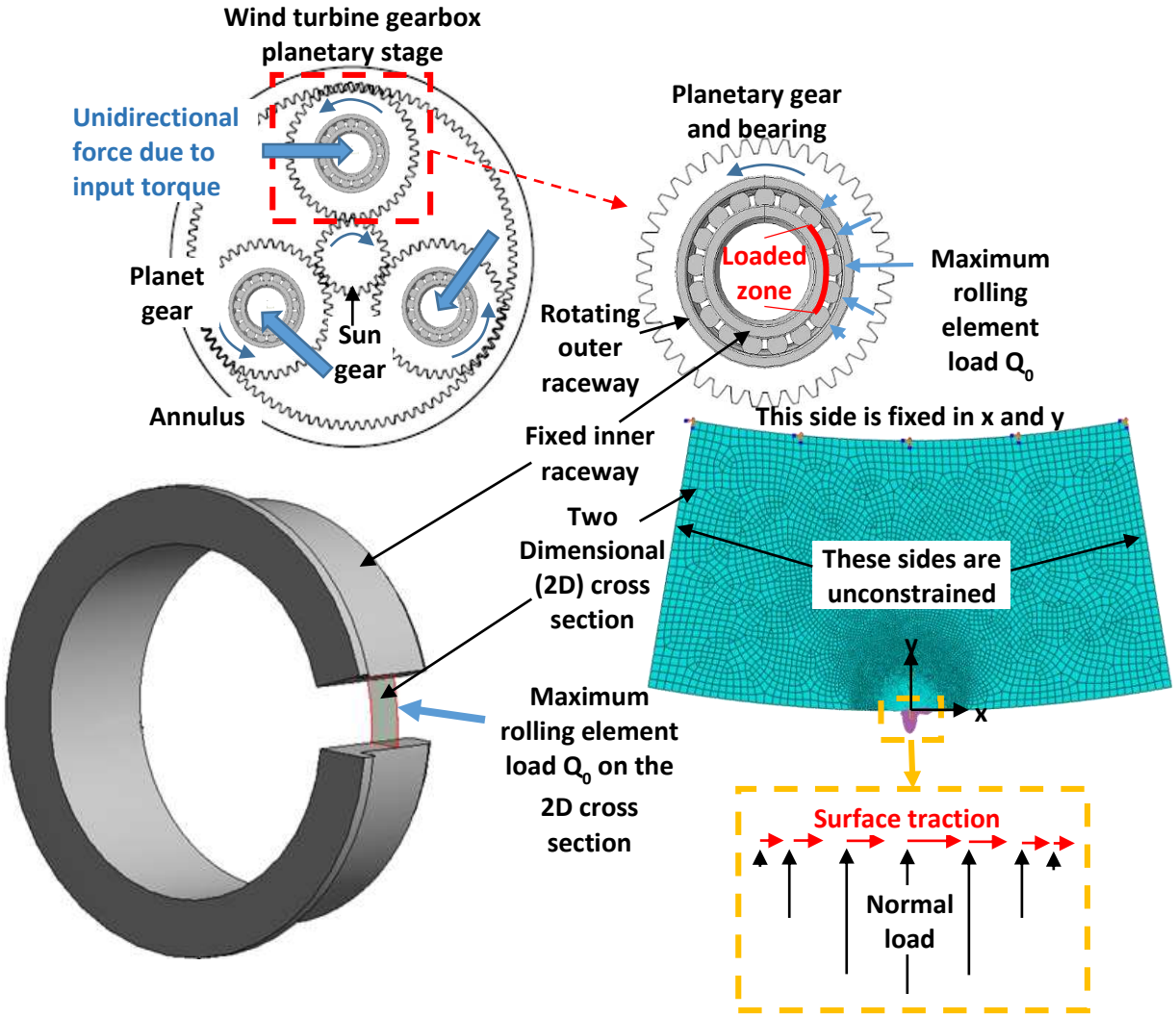

Figure 1: A wind turbine planetary stage and the loaded zone (failure zone) in the planetary bearings with Illustration for the modelled part, and the adopted boundary conditions and load distribution.

Table 1: Mechanical properties of bearing steel (AISA 52100, 100Cr6, EN31, JIS-SUJ2) [2][24][25][26]

Ultimate tensile strength (MPa)	Yield strength, $R_{p0.2}$ (MPa)	Vickers hardness HV	Elastic modulus E (GPa)
2150 – 2450	1400 – 2200	750 – 850	190 – 210

Table 2: The chemical composition of bearing steel (AISA 52100, 100Cr6, EN31, JIS-SUJ2) [25]

C	Mn	Si	Cr	Ni	Mo	Cu	S	P
0.95–1.10	0.2–0.5	0.15–0.35	1.30–1.60	0.0-0.3	0.0–0.03	0.025-0.3	0.025-0.11	0.0-0.05

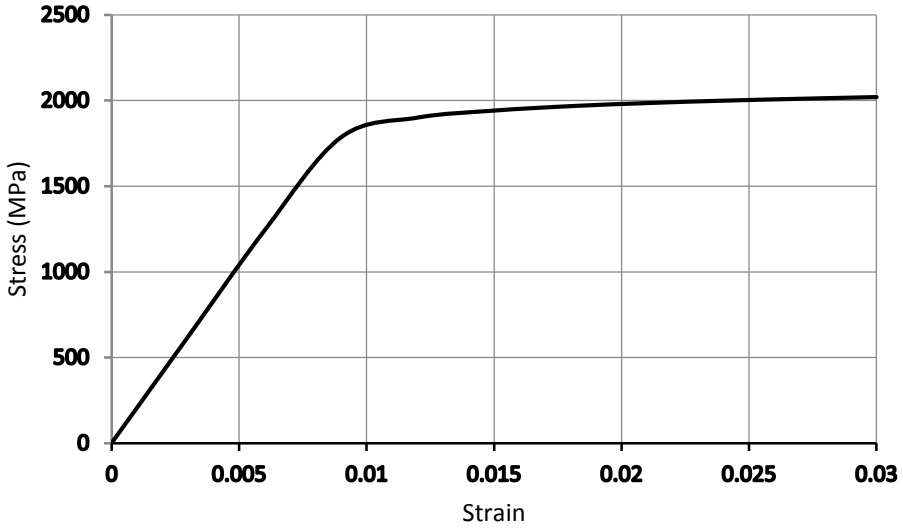

Figure 2: Stress-strain curve of bearing steel [24]**.**

For validation, the stress distributions under the surface were compared with that from the analytical solution represented by the line contact [27], as shown in Figure 3. The validation includes subsurface stresses at x=0 and x=0.9 * half width of contact (b), as shown in Figure 3. In this figure, the COT is the Coefficient Of Traction which represents the ratio of surface traction q to the normal contact pressure p. The maximum contact pressure p_{max}=1700 MPa was applied, since this value is close to the maximum contact pressure with torque reversal during shutdown [28]. Although higher contact pressure occurs during start up, the p_{max}=1700 MPa is closer to the maximum contact pressure during normal operation [29][30], which makes the results more conservative. This figure shows accurate results compared with the analytical solution within the elastic limit.

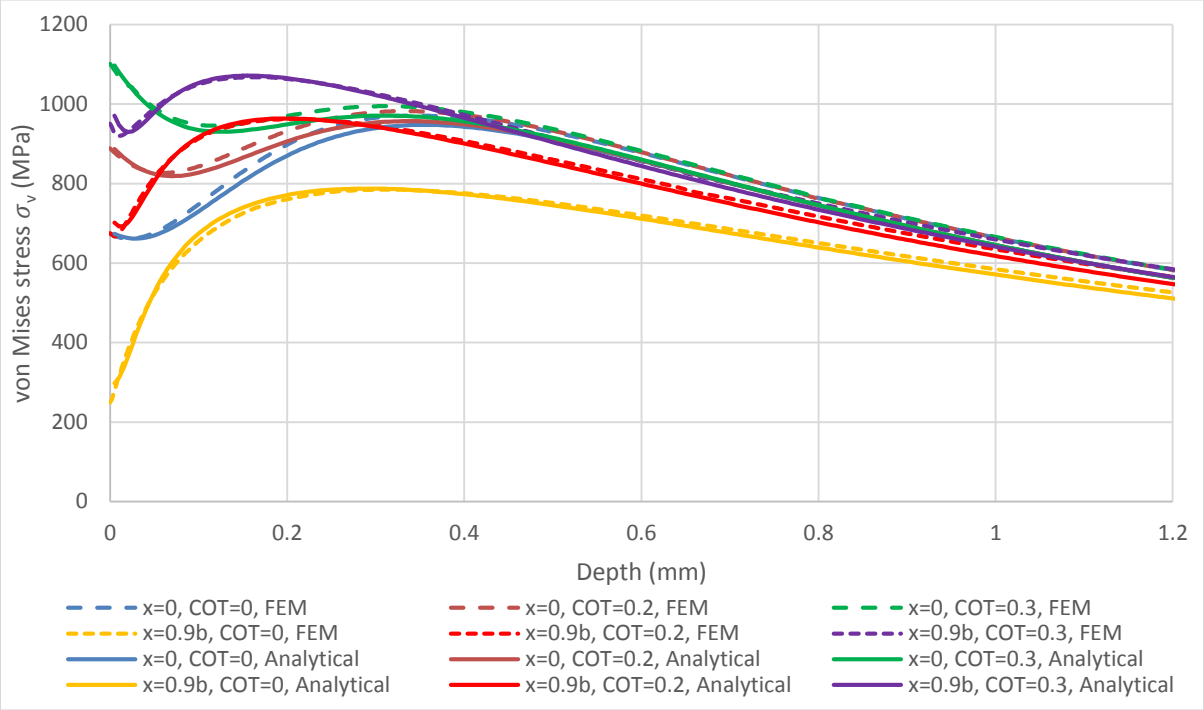

Figure 3: Validation of the FE models at different values of surface traction represented by the Coefficient Of Traction (COT). The p_{max} equals1700 MPa and b is the half width of contact.

2.2 Inclusion description:

The inclusion was modelled as a Type A (MnS) by an elliptical shape inclined by 45˚ to the Over Rolling Direction (ORD). Its dimensions as semi-minor and semi-major radii were9.6 μm and 28 μm, respectively. The centre of this inclusion was 80 μm from the surface and is exactly below the centre of the contact width at x=0. The properties of this inclusion used in the models were v=0.25 and E=108GPa as that averaged from 69-147 GPa [31][25]. Two types of modelling were utilized to simulate the inclusion-steel matrix interaction. In the first type, the inclusion was defined by a partition of different material properties perfectly bonded to the steel matrix in which no separation was allowed between the contacted bodies. The inclusion in the second type was modelled as a separate body with contact interaction between the inclusion and the steel matrix in which separation was allowed between the contacted bodies. The interaction was hard contact, to allow separation after contact but without penetration. This modelling for the interaction between the inclusion and the steel matrix aimed to mimic the non-perfect bonded or separated inclusion, as observed from the examination of a wind turbine planetary bearing [22]. A mesh sensitivity study was conducted using three models of different element size in the location of the inclusion and the contact area. The element sizes used in these models were 10 µm, 2 µm, and 0.5 µm respectively. It was found that reducing element size from 10 µm to 0.5 µm does not change the match between the FE solution and the analytical solution. In this study, an element size of 0.5 µm was chosen to improve the representation for the geometry of the elliptical shape of the inclusion and its gap with the steel matrix.

3 Local Effect of Inclusion for Different Steel Matrix Bonding

Two models were utilized, one with an embedded inclusion, and the other without in order to investigate the local effect of inclusions on subsurface stress distribution and concentration. One elongated MnS inclusion was embedded in a circumferential section of the inner raceway of a NREL 750 kW WT planetary bearing. A normal load with Hertzian distribution of p_{max}= 1700 MPa was used for both models, with and without inclusion. For the model with inclusion, the interface between the inclusion and the steel matrix was modelled in two ways as described in Section 2.2. Firstly, the

inclusion was modelled as perfectly bonded to the steel matrix; secondly, it was modelled as another body confined inside the steel matrix with contact interaction. Stress variation was found across the inclusion and at its tip along lines (a) and (b), as shown in Figure 4. The stress variation results are shown in Figure 5, and they clearly reveal local stress concentration around the inclusion without changing the stress distribution far from the inclusion., his local stress concentration shows that even soft inclusions such as MnS can still cause high stress concentrations which can initiate localised plastic deformation by comparing these stress values with the yield stress of the modelled steel, as shown in Section 2.2. Accordingly, the effect of inclusion bonding is very clear, showing that the separation may have a significant effect on the level of stress concentration.

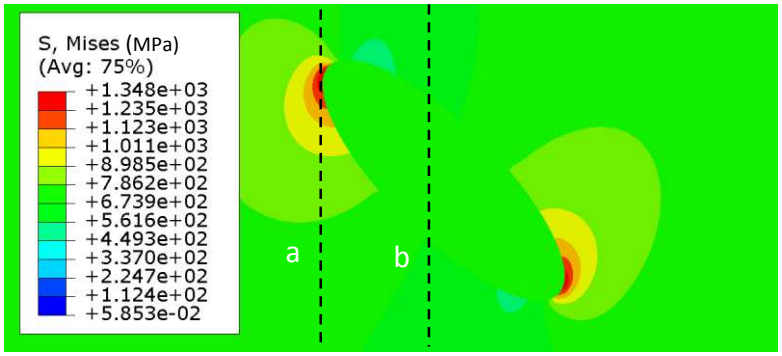

Figure 4: Paths for measuring the variation of σ_v at p_{max}=1700 MPa. Path (a) crosses the stress concentration near the tip of the inclusion, and path (b) crosses the inclusion (the contact surface is 80 μm below the inclusion).

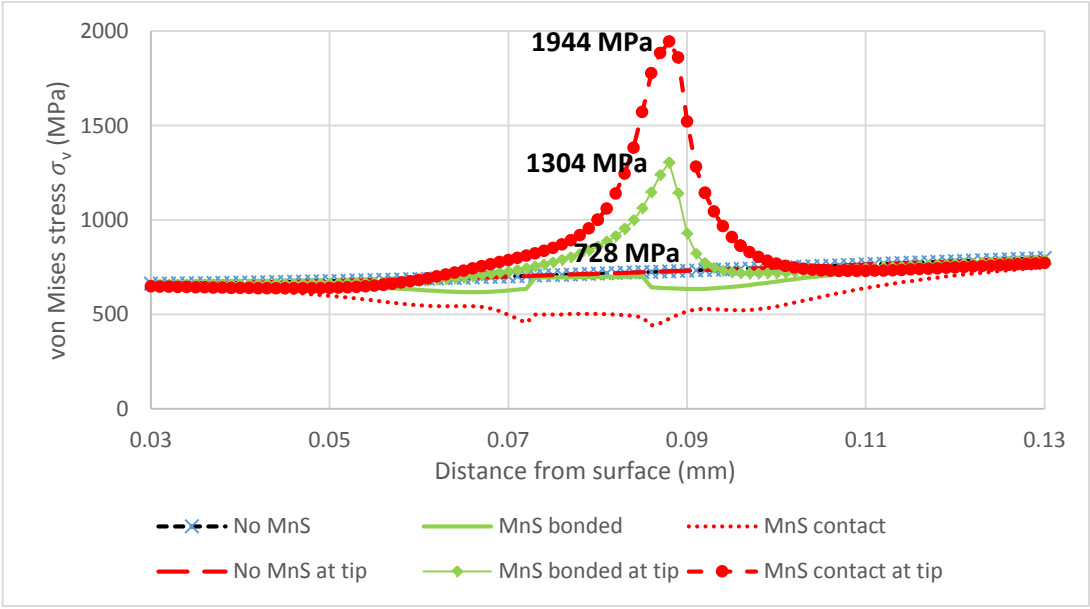

Figure 5: Local effect of the inclusion on the variation of von Mises stress (σ_v) under p_{max}=1700 MPa.

Even for the perfectly bonded MnS inclusion, the stress almost doubled at the tip, which highlights the importance of considering the inclusions for subsurface stress and damage calculations. The stress increase at the inclusion tip due to separation from the steel matrix, could make the yielding or stress induced transformation more feasible at lower contact pressure, than that expected if the inclusion effect is neglected. The local stress concentration around the tips of MnS inclusions could be correlated to the local microstructure alteration, such as WEA. However, this stress may not cause an observable microstructure alteration other than additional stress which is expected to be a beneficial

compression stress under loading. Nevertheless, during the unloading, the residual stress needs to be investigated, as discussed in the following section.

4 Effect of Normal and Tangential Loading-Unloading On Residual Stress

The load on each point on the raceways alternates between loading and unloading during the pass of each roller. A FE model with contact interaction between a MnS inclusion and the steel matrix was utilized to show the effect of loading-unloading - with and without surface traction - on the residual stress around inclusion tips. This kind of loading was modelled by a Hertzian pressure distribution that changed between zero and maximum, which was a simplification for the roller moving over the point of maximum load on the raceway.

A similarity between the stress distribution around the inclusion, and the butterfly wings pattern was observed during the variation of surface loading. At the maximum load p_{max}=1700 MPa without surface traction (q=0 MPa), the stress around the inclusion and inside it, is shown in Figure 6. At maximum loading, the stress exceeded the average yield limit for bearing steel of 1800 MPa presented in Table 1, as shown in Figure 7. The contour of equivalent stress, and the localized yielding show a similarity with the topography of the butterflies wings observed from the examination of the failed bearings. However, better matching is observed when a maximum surface traction of q_{max}=600 MPa is applied, as shown in Figure 8. Nevertheless, no crack opening at inclusion tip could be expected under loading since the principle stresses show compression, as shown in Figure 9. On the other hand, as shown in Figure 10, the high value of residual stress after removing the load shows tension at the inclusion tip which could stimulate and drive crack opening. Accordingly, the factors affecting the development of this stress were investigated.

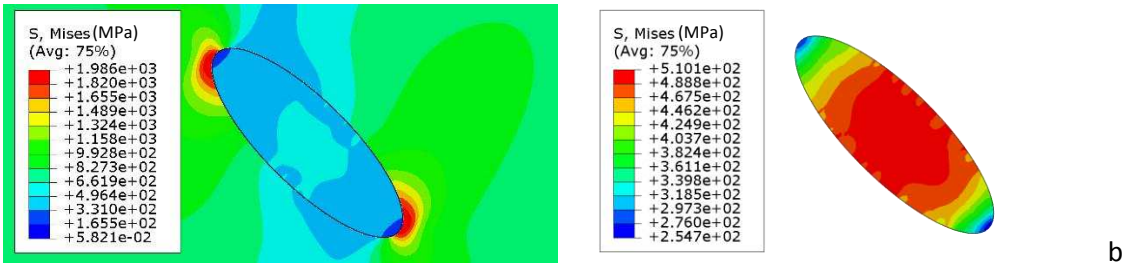

a b

Figure 6: Stress contours at p_{max}=1700 MPa and q=0 MPa. Figure (a) shows stress in matrix and inclusion and Figure (b) shows stress inside the inclusion only.

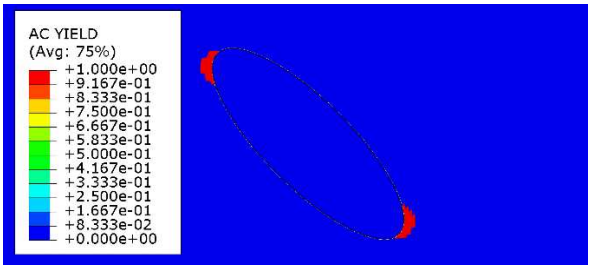

Figure 7: localized yielding at tips of MnS inclusion under p_{max}=1700 MPa and q=0 MPa

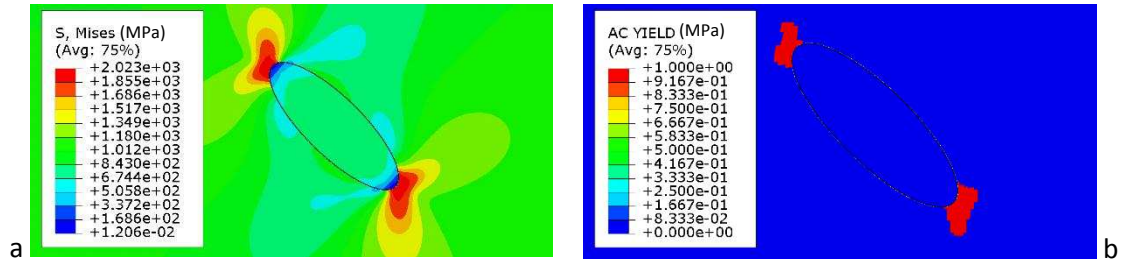

Figure 8: Stress contours and localized yielding at tips of MnS inclusion under p_{max}=1700 MPa and q_{max}=600 MPa. Figure (a) shows stress contours and Figure (b) shows the localized yielding.

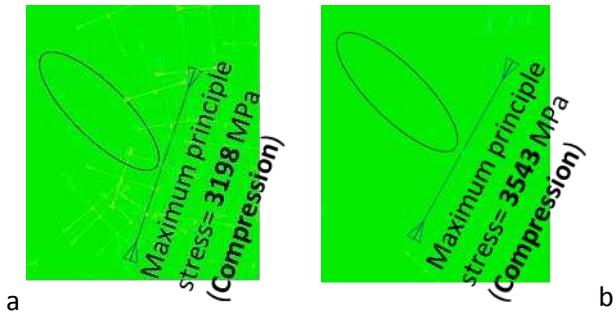

Figure 9: Compression stress at tips of MnS inclusion. Figure (a) shows stress under p_{max}=1700 MPa and Figure (b) shows stress under p_{max}=1700 MPa and q_{max}=600 MPa.

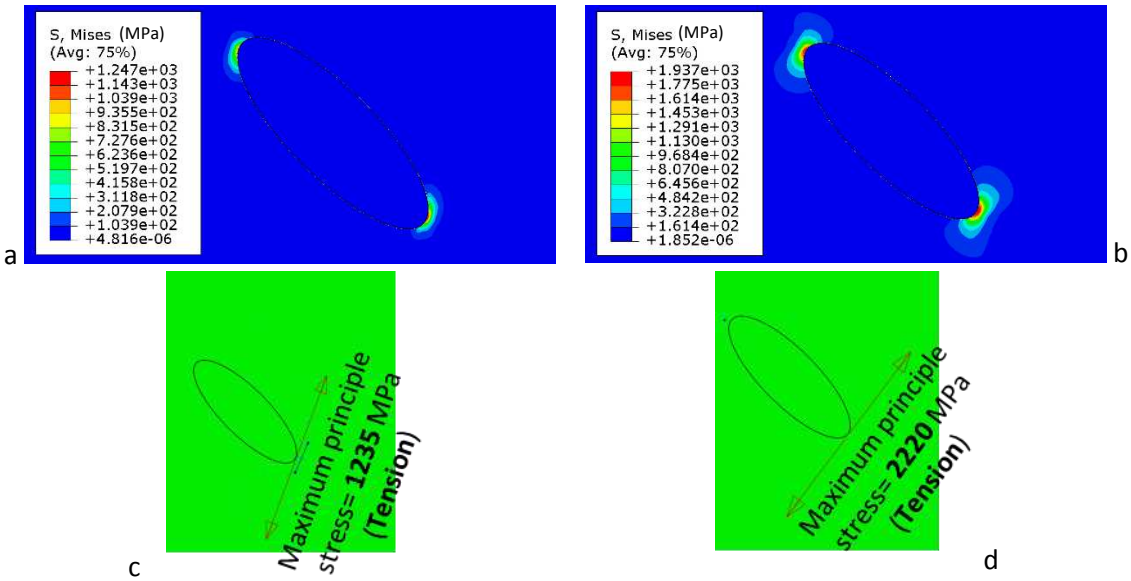

Figure 10: Tensile stresses at unloading. Figures (a) and (c) show stresses after loading of p_{max}=1700 MPa; and Figures (b) and (d) show stresses after loading of p_{max}=1700 MPa and q_{max}=600 MPa.

The effect of the inclusion-steel matrix interaction, and the value of p_{max} and q_{max} on residual stress around the inclusion tips were investigated. It was observed that no residual stress was developed when the inclusion was modelled with perfect bonding to the steel matrix. This highlights the role of the separation between the inclusion and the steel matrix as a non-perfect bonding, or a gap attached to the inclusion as observed from the examination of the failed bearings. The effect of surface traction on the value of residual stress is very clear, as shown in Figure 10. To compare the effect of high surface

traction and high normal load, another model with a normal load only of Hertzian distribution with p_{max}=3000 MPa was developed to investigate the effect on the residual stress. The results of this model, as shown in Figure 11, showed almost the same residual tensile stresses as from p_{max}=1700 MPa and q_{max}=600 MPa in Figure 10. This result supports the occurrence of subsurface damage due to high surface traction rather than high normal load. The reason for this is that the results from previous studies, such as [32], did not show the contact pressure reaching a very high value, such as 3000 MPa, while surface traction is confirmed from the metallurgical examinations [22]. Additionally, in the following section, a comparison between the observed butterfly wings, and the inclination of the stress concentrations around the inclusion will be made to support the occurrence of surface traction.

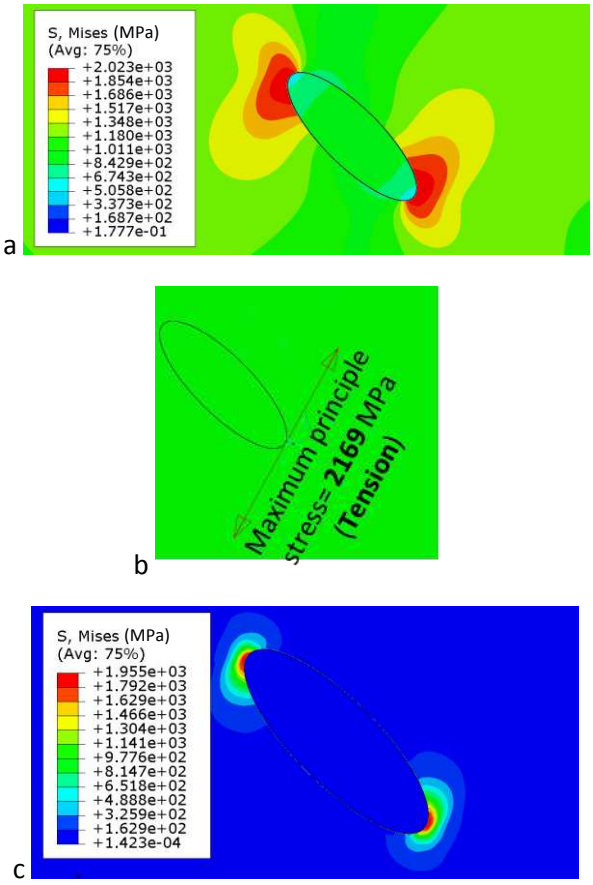

Figure 11: (a) Equivalent stress at p_{max}=3000 MPa , (b) Principle stress at unloading, and (c) Equivalent stress at unloading.

The stress distribution during maximum loading could explain the microstructural change in the form of WEA, and the tensile stress during unloading could explain the crack opening at the inclusion tip where there is a separation between the inclusion and the bearing steel. These results could solve the dilemma of explaining the sequence of WEA and the associated micro-crack in the observed butterfly wings. The rubbing theory to explain the relationship between the WEA and the associated cracks, assumes the occurrence of the cracks first, and the WEA is generated by the rubbing between the crack faces under loading-unloading conditions [33]. Although the evolution of the WEA in this mechanism may happen - and it cannot be proved or disproved using the current model - the crack opening at inclusion tips under compression load only may not be possible under facture mode I, as shown in Figure 9. This finding can be supported by a previous study that shows that the micro-plastic strain of bearing steel occurs under less load in tension than in compression [34]. Accordingly, the separation between the inclusion, and the steel and the occurrence of tensile stress at unloading, are essential for crack opening under mode I. Also, the effect of repeated cyclic loading on the

development of the residual plastic strain, that could be related to the microstructural change and crack opening will be discussed in Section 5.

5 Effect of Cyclic Loading

The evolution of maximum equivalent stress, residual stress and equivalent plastic strain under a number of loading-unloading cycles was investigated. Repeating the loading/unloading for a number of cycles was applied in a model with p_{max}=1700 MPa and q_{max}=320 MPa, which is equivalent to COT=0.188. This value of COT is not extremely high, and keeps the maximum stress under the surface. The amplitude of normal and tangential load was varied between zero and maximum during ten identical cycles, as shown in Figure 12, where the p_{max} and q_{max} at any time was 1700 MPa*Amplitude and 320 MPa*Amplitude, respectively. In order to define the ten cycles of loading-unloading, the time period defined in this simulation is divided into ten equal intervals. The value of the time period does not affect the simulation since the model is quasi-static and it is only used to enable tracking the change of the results at each load cycle. The letters in this figure are utilized to discuss the variation of maximum von Mises stress (σ_v) and its residual stress in Figures 13, and the equivalent plastic strain (PEEQ) in Figure 14. It was found that σ_v at maximum load decreases while the residual stress increases with increasing the number of cycles, as shown in Figure 13. This may justify the accumulated stress or strain induced phase transformation such as WEA. The increase in the equivalent plastic strain and residual stress can be explained by the ratchetting mechanism.

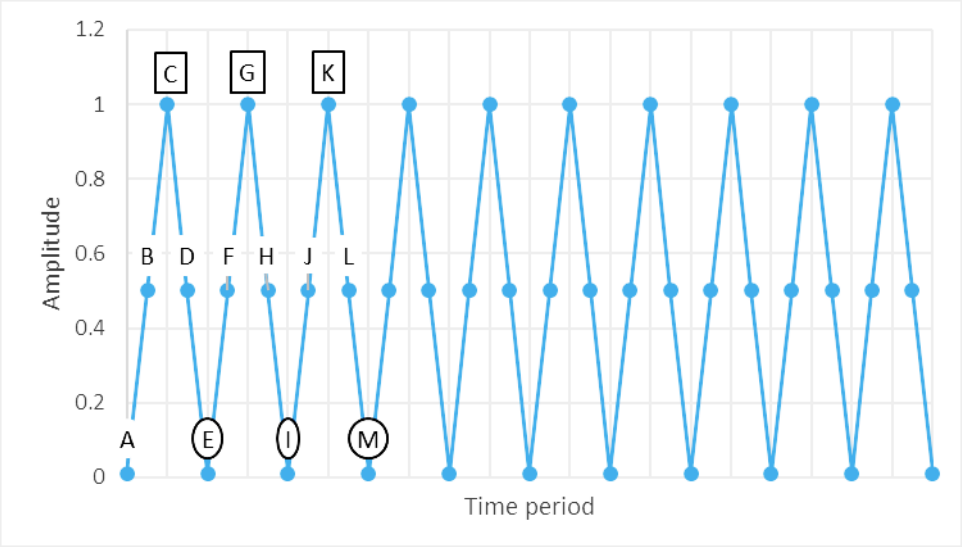

Figure 12: Cyclic amplitude of normal and tangential load to represent cyclic loading on bearing raceways.

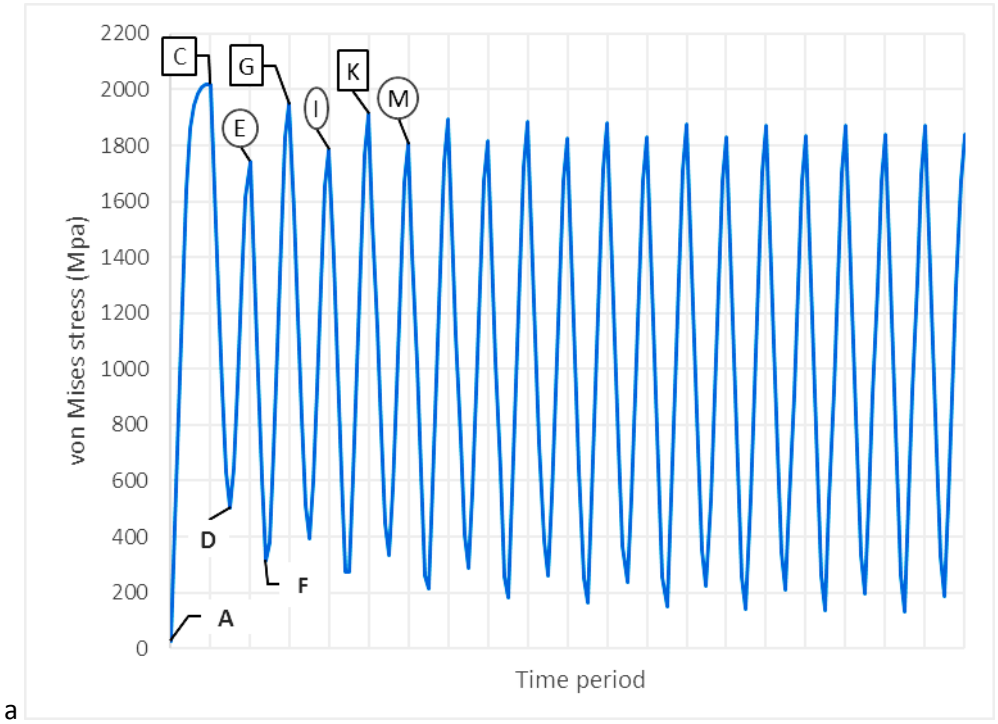

a

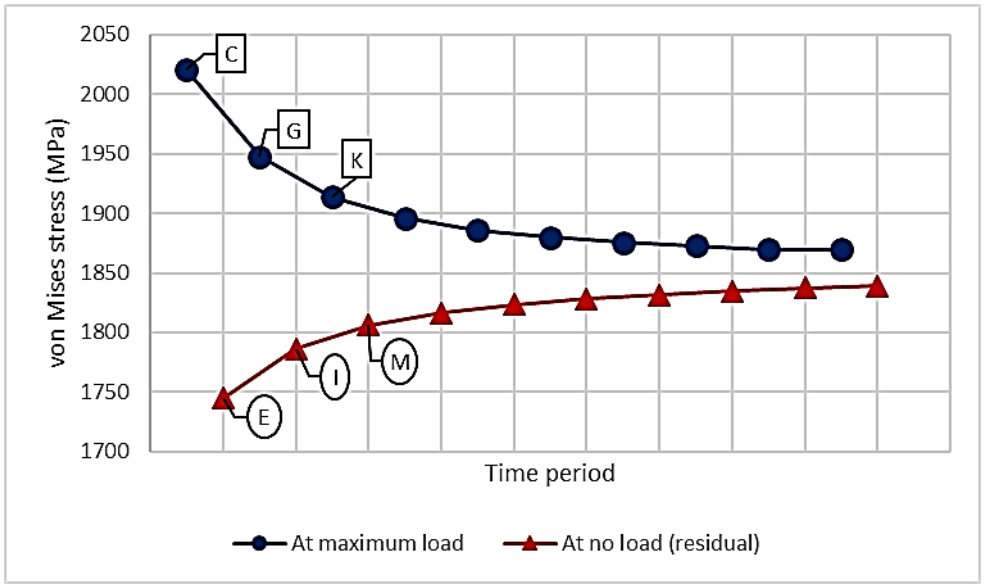

b

Figure 13: (a) Stress variation at the inclusion tip due to the load amplitude variation shown in Figure 12 with p_{max}=1700 MPa and q_{max}=320 MPa. In this figure, point A is the stress at no load and no residual stress; point C is the stress when the load reaches its maximum value (p_{max}); point D is the stress when the load during the unloading reaches $p_{max}/2$, at this point the residual stress starts to build-up ; E is the stress point when the load during unloading reaches zero, at this point the residual stress reaches its maximum value for this load cycle; and F is the stress when the load during the loading of the second loading cycle reaches $p_{max}/2$. (b) Stress at maximum load and residual stress at no load.

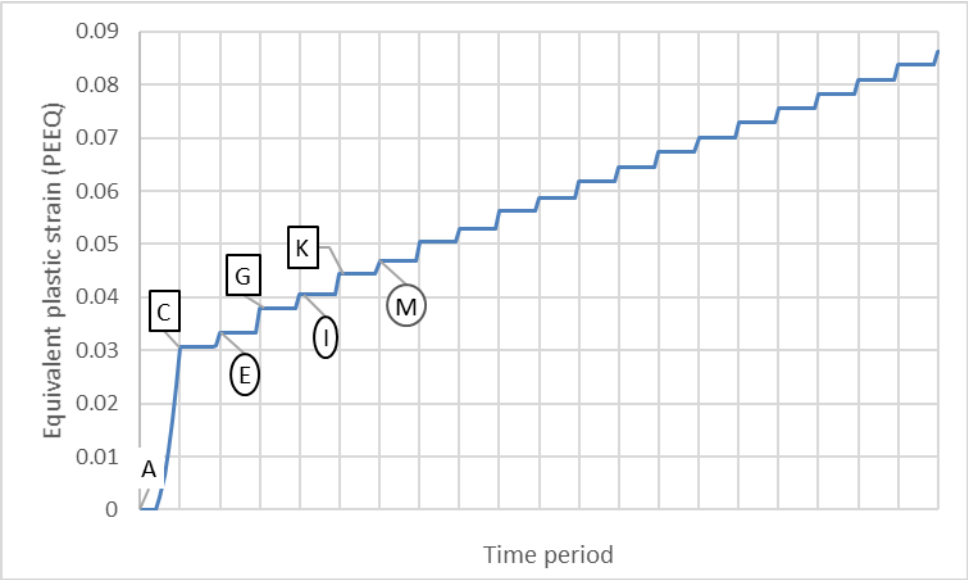

Figure 14: Equivalent plastic strain at inclusion tip due to the load amplitude variation shown in Figure 12 with normal load of p_{max}=1700 MPa and surface traction of q_{max}=320 MPa (the upper case letters have a similar representation in Figure 13).

To show the effect of surface traction during cyclic loading, the results in Figures 13 and 14 were compared with that from another model, where only a normal load was applied. The same amplitude shown in Figure 12 was used with p_{max}=1700 MPa. The results of equivalent stress σ_v and equivalent plastic strain are shown in Figures 15 and 16 respectively. The values and the variation of residual stress and the equivalent plastic strain, are much higher when there are normal and tangential forces on the surface. Accordingly, any stress or strain induced microstructure alteration, such as WEA, will be much faster if surface traction occurs. Also, the higher tensile residual stress makes crack opening more likely to occur.

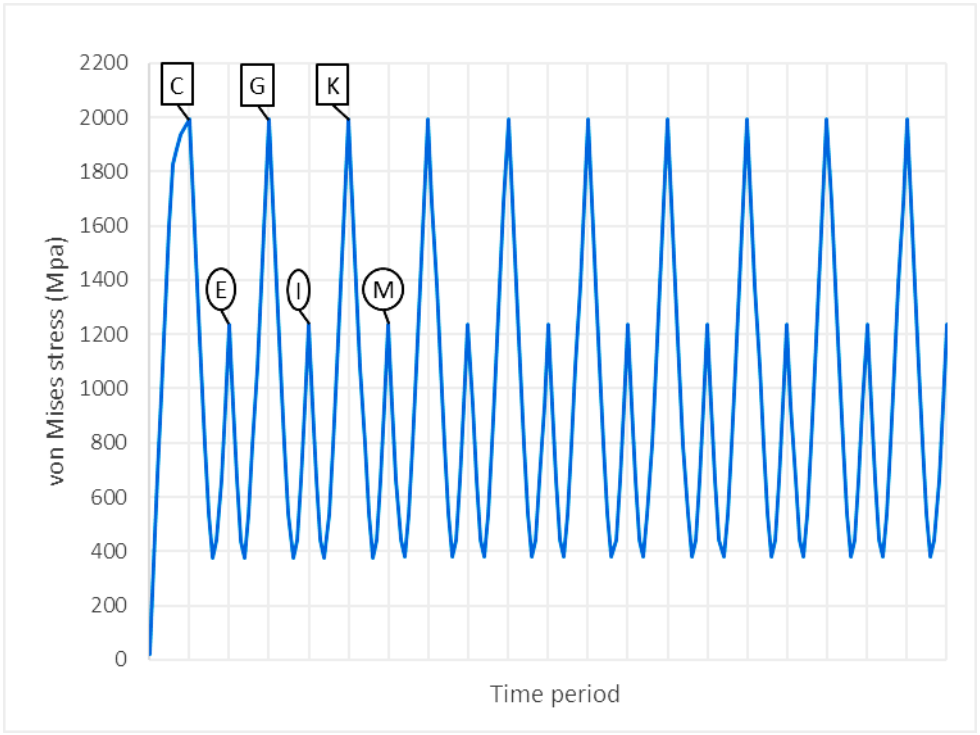

a

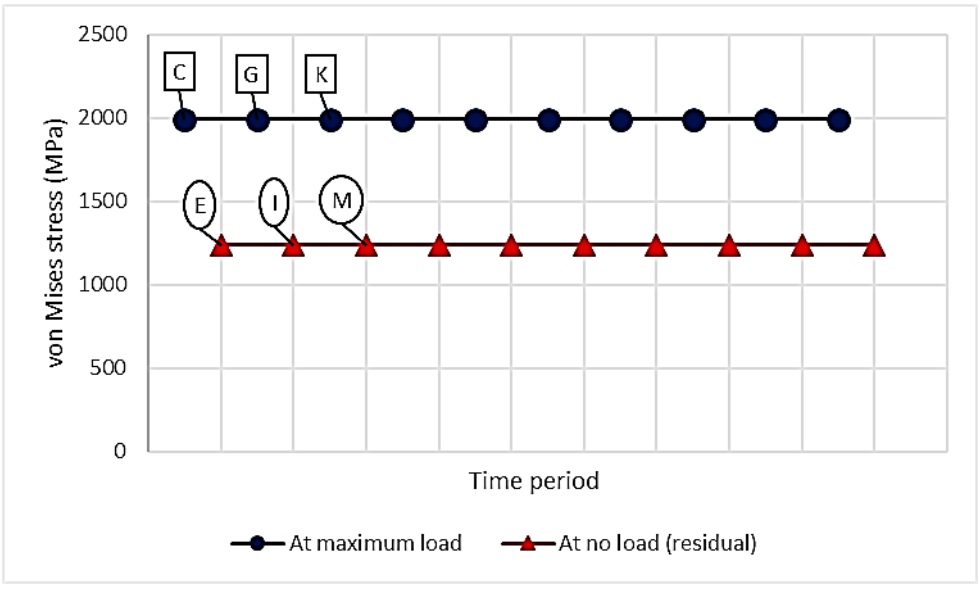

b

Figure 15: (a) Stress variation at inclusion tip during cyclic loading with the peaks and valleys having similar representation to that in Figure 13 (the load amplitude applied is shown in Figure 12 and p_{max}=1700 MPa). (b) Stress at maximum load and residual stress at no load.

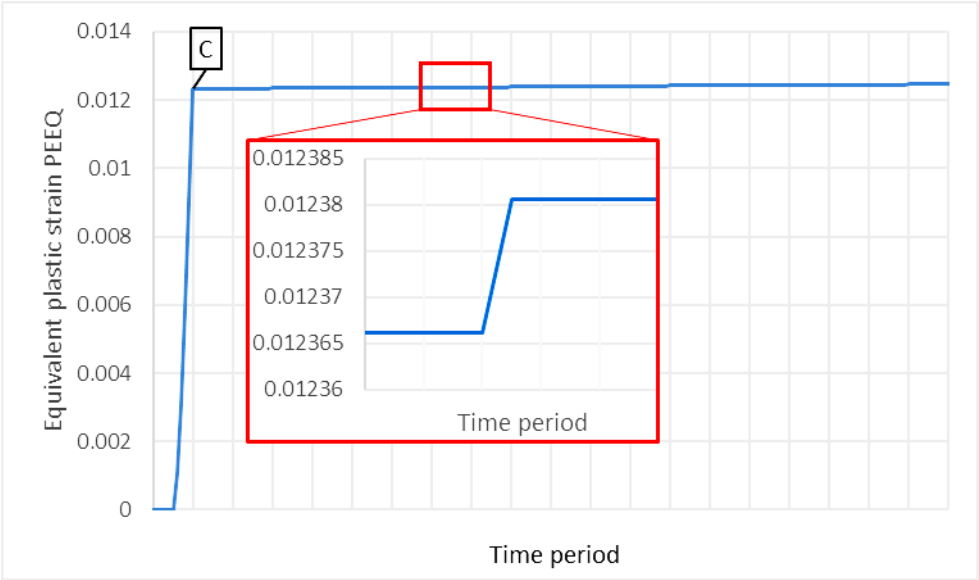

Figure 16: Equivalent plastic strain at inclusion tip without surface traction during cyclic loading. The highlighted part of the curve shows the stepwise increase of the PEEQ as in Figure 14, but with smaller rate (the load amplitude applied is shown in Figure 12 and p_{max}=1700 MPa).

6 Comparison with Butterflies Wings Observed in a Wind Turbine Gearbox Bearing Using Different Surface Traction Directions

The surface traction was shown in the previous section to have a significant effect on the stress and strain around the inclusion. The possible cause of surface traction in WTGBs was investigated by correlating the direction of surface traction, to the inclination direction of the observed butterflies wings in the failed bearings. Two models were developed with a Hertzian distribution of normal contact pressure, and a tangential surface traction of p_{max}=1700 MPa and q_{max}=600 MPa. Each of these models has an embedded MnS inclusion with a contact interaction between this inclusion and the steel matrix. These models are identical, except for the direction of the surface traction, as shown in Figure 17. The load amplitude in both models was varied between maximum and minimum to simulate the loading/unloading on the raceway, as explained in Section 4. At maximum load the stress around the inclusions is shown in Figure 18; and for unloading the residual stress and equivalent plastic strain are shown in Figure 19. These results show clearly the significant effect of the traction direction on residual stress and equivalent plastic strain, if an elongated inclusion with a certain angle is considered. To demonstrate the stress distribution around a perfectly rounded stress riser, two similar models were developed, but here the inclusions were replaced by a circular void of 2 microns radius. The results of these models as shown in Figure 20 illustrate identical symmetry around the diagonal axis regardless of the surface traction direction, which was not the case for the elliptical inclined inclusion. Accordingly, this observation can be used to predict the direction of the surface traction in WT planetary bearings, and hence the occurrence of sliding or reversed rotation.

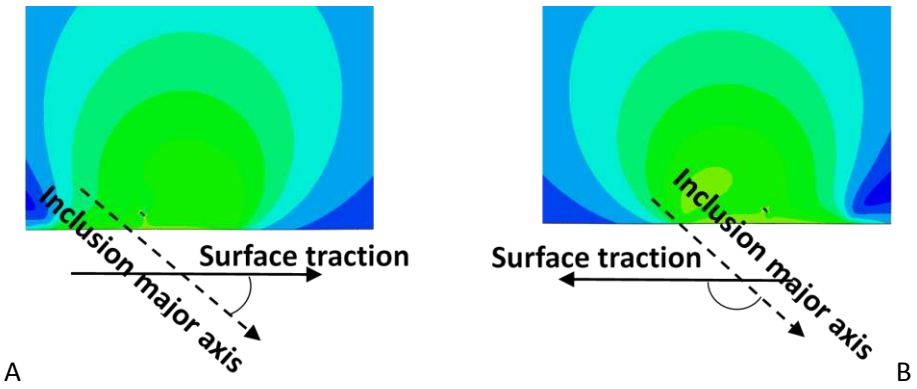

Figure 17: The Modelling types (A and B) used to investigate the effect of surface traction direction on stress and strain at inclusion tips. In these models, p_{max} equals 1700 MPa and q_{max} equals 600 MPa.

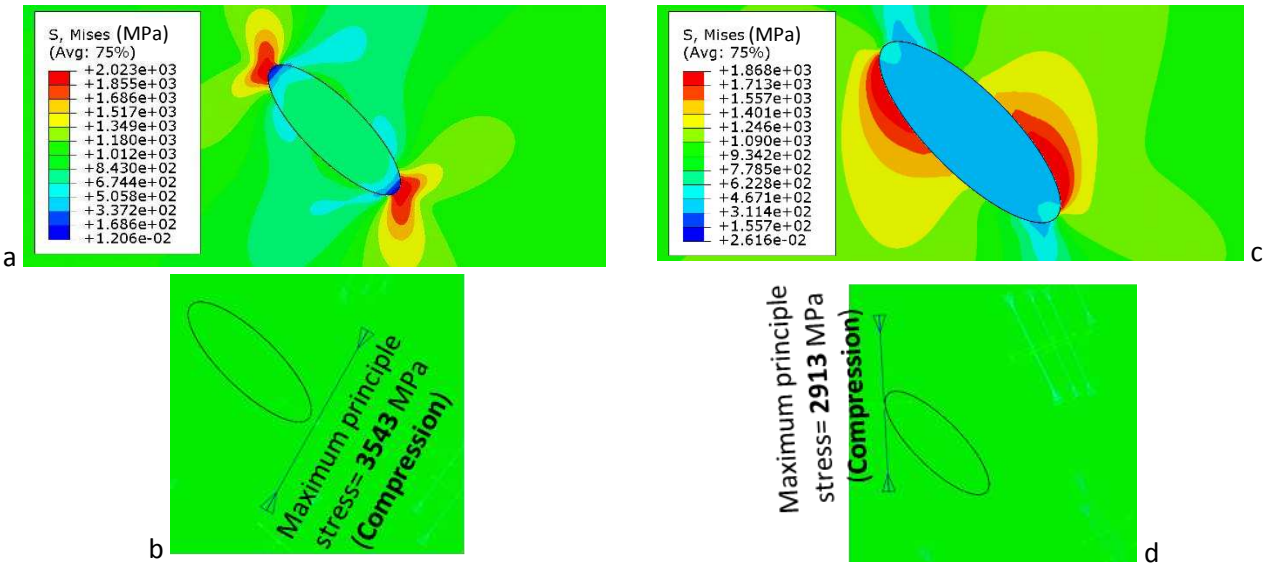

Figure 18: Stress at maximum load from the models in Figure 17. Figures (a) and (b) result from model (A); and Figures (c) and (d) result from model (B).

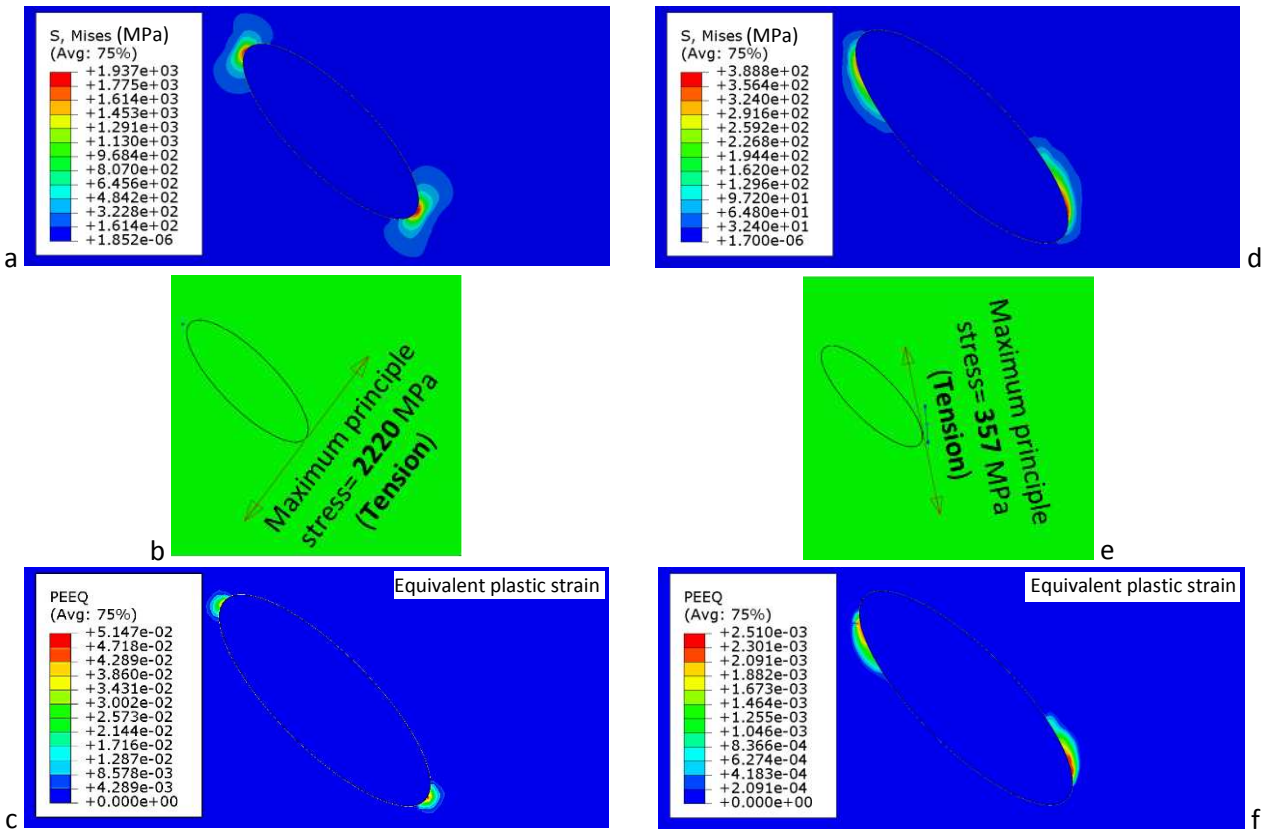

Figure 19: Residual stress and equivalent plastic strain at unloading based on the models in Figure 17. Figures (a) to (c) result from model (A); and Figures (d) to (f) result from model (B).

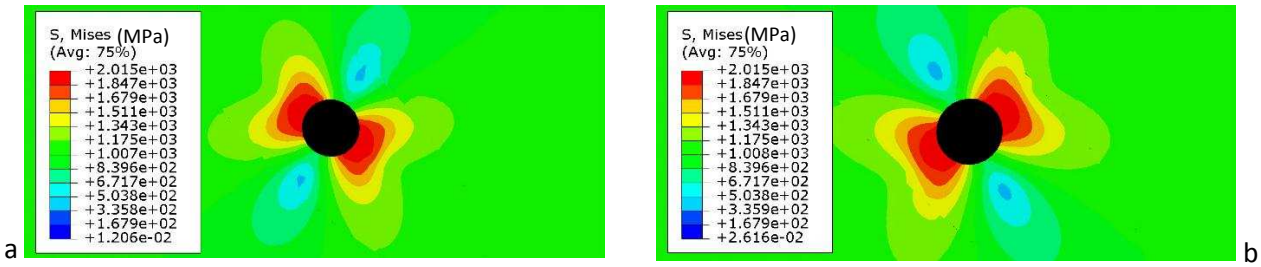

Figure 20: Illustrations for stress around 2 µm circular gap under different directions of surface traction, shown in Figure 17. Figure (a) results from model (A); and Figure (b) results from model (B).

Different surface traction directions can make either an acute or an obtuse angle with the inclusion's major axis, (i.e. the line that links the initiation points of the butterfly wings), as shown in Figure 17. When this angle is acute, as in Figures 17 (a) and (b), and Figure 19 (a) to (c), the stress concentration around the inclusion tips matches the feature of butterflies wings better, specifically the inclination angle of the butterfly wings. Figure 21 shows some of the observed butterflies wings and the ORD in uncoated and Black Oxide (BO) coated bearings [22][35][5]. If no sliding is assumed between rollers and races, the direction of surface traction should be complementary/opposite to the rolling direction. However, it was found that this pure rolling results in an obtuse angle between this surface traction and the line that links the initiation points of the butterfly wings, as shown in Figure 21. Thus, lower stress and plastic strain occur at the inclusion tip, as shown in Figure 17 and 19. On the other hand, the surface traction due to sliding or reversed rotation makes an acute angle with the inclusion's major axis which results in high stress and plastic strain at the inclusion tips, as shown in Figure 17 and 19. This finding highlights the occurrence of high surface traction in WT planetary bearings, which could be due to sliding or reversed rotation.

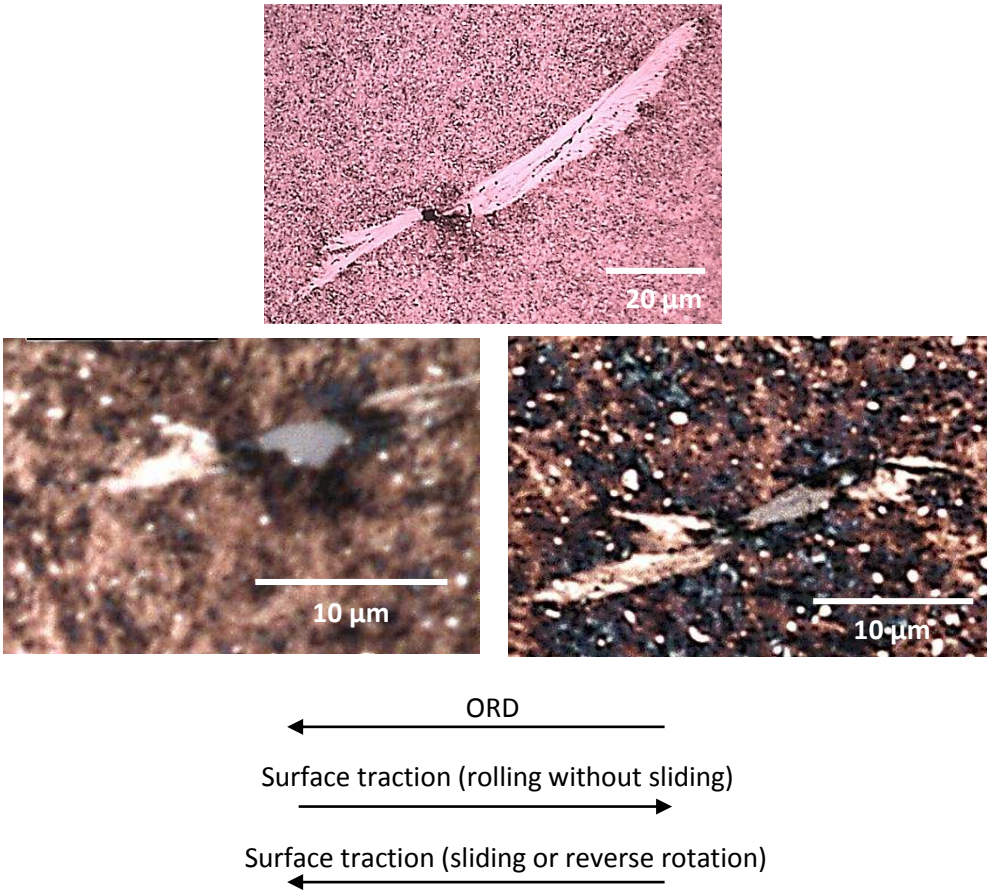

Figure 21: Butterfly wings angle relative to the rolling direction (surface of contact is below the butterflies).

7 Conclusions

The damage initiation at MnS inclusion was investigated using FE modelling and correlations of the results with observations from failed wind turbine gearbox bearings. The following conclusions can be drawn from the present investigation:

1. It was found that stress concentration contours and localized yielding around the tips of the modelled inclusion resemble the WEA in the butterflies wings. This local stress distribution is similar to the distribution of butterflies wings observed in examined bearings. It was also observed that a surface traction in the ORD, which can occur due to reversed rotation or sliding, increases the similarity between the WEA in the butterflies wings, and the stress distribution at inclusion tips.
2. In the modelling of a MnS inclusion, the separation between the inclusion and the steel matrix shows a significant effect on the stress concentration with an increase of 167%. However, even for the perfectly bonded MnS inclusion the stress level is almost doubled at the tips with an increase of 79.1%, which highlights the importance of considering the inclusions for subsurface stress calculations.
3. It was found that, in addition to the compression stress during loading, tensile residual stress and equivalent plastic strain were generated around the tips of the inclusion when a gap was modelled between the inclusion and the steel matrix. The tensile residual stress is 38.6% of the compression stress under normal load only of p_{max}=1700 MPa, and it reaches 62.7% under

normal and tangential load of p_{max}=1700 MPa and q_{max}=600 MPa respectively. However, no residual stress was developed when the inclusion was modelled as perfectly bonded with the steel matrix. The tensile residual stress increases with cyclic loading by a rate of 5.5% for the first ten cycles under normal and tangential load of p_{max}=1700 MPa and q_{max}=320 MPa respectively. Surface traction that makes an acute angle with the inclusion's major axis increases the tensile residual stress by 465%, comparing with the obtuse angle, under normal and tangential load of p_{max}=1700 MPa and q_{max}=600 MPa respectively. Accordingly, specific surface traction value and direction can accelerate crack opening and any stress or strain induced microstructure alteration, such as WEA.

4. Correlating the results of FE modelling and the inclination of the butterfly wings suggests the occurrence of reversed rotation or sliding in the ORD between the contact surfaces which causes high surface traction that makes acute angle with inclusion's major axis.

References

[1] K. S. Scott, D. Infield, N. Barltrop, J. Coultate, and A. Shahaj, "Effects of Extreme and Transient Loads on Wind Turbine Drive Trains," *Proc. 30th ASME Wind Energy Symp.*, pp. 1–24, 2012.

[2] M.-H. Evans, "White structure flaking (WSF) in wind turbine gearbox bearings: effects of 'butterflies' and white etching cracks (WECs)," *Mater. Sci. Technol.*, vol. 28, no. 1, pp. 3–22, Jan. 2012.

[3] a. Ruellan, F. Ville, X. Kleber, a. Arnaudon, and D. Girodin, "Understanding white etching cracks in rolling element bearings: The effect of hydrogen charging on the formation mechanisms," *Proc. Inst. Mech. Eng. Part J J. Eng. Tribol.*, vol. 228, no. 11, pp. 1252–1265, 2014.

[4] K. Stadler and A. Stubenrauch, "Premature bearing failures in industrial gearboxes," *Annu. Rev. Mater. Sci.*, vol. 9, no. 1, pp. 283–311, 2013.

[5] H. A. Al-Tameemi, H. Long, and R. S. Dwyer-Joyce, "Damage characterisation of white etching cracks in a black oxide coated wind turbine gearbox bearing," *Wear*, 2019.

[6] A. D. Richardson, M. ‐H. Evans, L. Wang, R. J. K. Wood, M. Ingram, and B. Meuth, "The Evolution of White Etching Cracks (WECs) in Rolling Contact Fatigue ‐ Tested 100Cr6 Steel," *Tribol. Lett.*, vol. 66, no. 1, pp. 1–23, 2018.

[7] B. Gould and A. Greco, "The Influence of Sliding and Contact Severity on the Generation of White Etching Cracks," *Tribol. Lett.*, vol. 60:29, no. 2, pp. 1–13, 2015.

[8] B. Gould and A. Greco, "Investigating the Process of White Etching Crack Initiation in Bearing Steel," *Tribol. Lett.*, vol. 62:26, no. 2, pp. 1–14, 2016.

[9] P. Rycerz, A. Olver, and A. Kadiric, "Propagation of surface initiated rolling contact fatigue cracks in bearing steel," *Int. J. Fatigue*, vol. 97, pp. 29–38, 2017.

[10] B. Gould, A. Greco, K. Stadler, E. Vegter, and X. Xiao, "Using advanced tomography techniques to investigate the development of White Etching Cracks in a prematurely failed field bearing," *Tribol. Int.*, vol. 116, pp. 362–370, 2017.

[11] J. Gegner, "Tribological Aspects of Rolling Bearing Failures," in *In: C.-H. Kuo (ed.), Tribology–Lubricants and Lubrication*, Rijeka, Croatia: InTech, 2011, pp. 33–94.

[12] T. Bruce, E. Rounding, H. Long, and R. Dwyer-Joyce, "Characterisation of white etching crack damage in wind turbine gear- box bearings," *Wear*, vol. 338–339, pp. 164–177, 2015.

[13] A. Greco, "Bearing Reliability-White Etching Cracks (WEC)," in *Gearbox Reliability*

Collaborative Annual Meeting, 2014.

[14] H. Uyama, "The mechanism of white structure flaking in rolling bearings," *Natl. Renew. energy Lab. Wind turbine*, pp. 1–37, 2011.

[15] H. Uyama, H. Yamada, H. Hidaka, and N. Mitamura, "The Effects of Hydrogen on Microstructural Change and Surface Originated Flaking in Rolling Contact Fatigue," *Tribol. Online*, vol. 6, no. 2, pp. 123–132, 2011.

[16] J. Gegner and W. Nierlich, "Tribology Seminar Wind Turbine A Recap Tribology Seminar," in *NREL Wind Turbine Tribology Seminar*, 2011.

[17] K. Hiraoka, M. Nagao, and T. Isomoto, "Study on flaking process in bearings by white etching area generation," *J. ASTM Int. STP 1465*, vol. 3, no. 5, pp. 234–241, 2006.

[18] N. Weinzapfel, F. Sadeghi, and V. Bakolas, "An Approach for Modeling Material Grain Structure in Investigations of Hertzian Subsurface Stresses and Rolling Contact Fatigue," *J. Tribol.*, vol. 132: 04140, no. 4, 2010.

[19] L. A. Mobasher Moghaddam. S, Sadeghi. F, Weinzapfel. N, "A Damage Mechanics Approach to Simulate Butterfly Wing Formation around Non-Metallic Inclusions," *ASME J. Tribol.*, vol. 137: 01140, no. 1, 2014.

[20] S. M. Moghaddam, F. Sadeghi, K. Paulson, N. Weinzapfel, M. Correns, and M. Dinkel, "A 3D numerical and experimental investigation of microstructural alterations around non-metallic inclusions in bearing steel," *Int. J. Fatigue*, vol. 88, pp. 29–41, 2016.

[21] A. D. Anoop, A. S. Sekhar, M. Kamaraj, and K. Gopinath, "Modelling the mechanical behaviour of heat-treated AISI 52100 bearing steel with retained austenite," *Proc. Inst. Mech. Eng. Part L J. Mater. Des. Appl.*, vol. 232, no. 1, pp. 44–57, 2018.

[22] H. A. Al-Tameemi, H. Long, and R. S. Dwyer-Joyce, "Initiation of sub-surface micro-cracks and white etching areas from debonding at non-metallic inclusions in wind turbine gearbox bearing," *Wear*, vol. 406–407, no. January, pp. 22–32, 2018.

[23] M. Cerullo, "Sub-surface fatigue crack growth at alumina inclusions in AISI 52100 roller bearings," *Procedia Eng.*, vol. 74, pp. 333–338, 2014.

[24] Totalmateria, "Bearing steel." [Online]. Available: http://www.totalmateria.com/.

[25] H. K. D. H. Bhadeshia, "Steels for bearings," *Prog. Mater. Sci.*, vol. 57, no. 2, pp. 268–435, 2012.

[26] A. Konrad, W. Nierlich, and J. Gegner, "Finite Element Analysis of the Rolling-Sliding Contact of Vibrationally Loaded Bearings Based on a Micro Friction Model," *Mater. Sci. Forum*, vol. 768–769, pp. 714–722, 2014.

[27] E. McEwen, "stresses in elastic cylinders in contact along a generatrix," *Philos. Mag.*, vol. 40, no. 454, 1949.

[28] H. Al-Tameemi, H. Long, and R. S. Dwyer-Joyce, "Investigation of wind turbine gearbox bearing subsurface damage considering transient loading and the seperation of MnS inclusions," *Wind. Summit 2016*, p. 145, 2016.

[29] BS-EN-61400-4, *Wind turbines Part 4: Design requirements for wind turbine gearboxes*. BSI Standards Publication, 2013.

[30] "American National Standard, ANSI/AGMA/AWEA 6006-A03: standard for design and specification of gearbox of wind turbines," *ANSI/AGMA/AWEA 6006-A03*, 2004.

[31] Y. Murakami, *METAL FATIGUE: EFFECTS OF SMALL DEFECTS AND NONMETALLIC INCLUSIONS*,

1st ed. 2002.

[32] T. Bruce, H. Long, and R. S. Dwyer-Joyce, “Dynamic modelling of wind turbine gearbox bearing loading during transient events,” *IET Renew. Power Gener.*, vol. 9, no. 7, pp. 821–830, 2015.

[33] R. H. Vegter, J. T. Slycke, J. Beswick, and S. W. Dean, “The Role of Hydrogen on Rolling Contact Fatigue Response of Rolling Element Bearings,” *J. ASTM Int.*, vol. 7: 102543, no. 2, 2010.

[34] A. Vincent *et al.*, “From white etching areas formed around inclusions to crack nucleation in bearing steels under rolling contact fatigue,” in *Bearing Steels: Into the 21st Century, ASTM STP 1327*, 1998, pp. 109 – 123.

[35] Hamza Al-Tameemi, “Effect of Surface Traction and Non-Metallic Inclusions on the Premature Failure of Wind Turbine Gearbox Bearings,” The University of Sheffield, 2017.